

Dimensional transport crossovers in thermoelectrics revealed by a simple transport model

Received: 5 August 2025

Accepted: 29 October 2025

Published online: 11 December 2025

Check for updates

Xiaoxuan Zhang^{1,2}, Thomas C. Chasapis³, Kaiqing Lu^{1,2,4,5},
Maxwell Thomas Dylla³, Meizhu Huang^{1,2}, G. Jeffrey Snyder³ & Yue Lin^{1,2}

Quantum confinement gives low-dimensional materials distinctive electronic behaviour, but assessing their effective band structure dimensionality (D) is difficult. Conventional probes such as angle-resolved photoemission spectroscopy (ARPES) or scanning tunneling microscopy (STM) demand ultra clean surfaces and expensive facilities. We introduce a generalized transport model that functions as an internal dimensionality meter: by tracking how the Seebeck coefficient varies with carrier concentration or temperature, we deduce D from two scaling laws, $S \propto (\frac{D}{2}) \ln T$ in non-degenerate regimes (e.g. $|S| \geq 200 \mu\text{VK}^{-1}$) and $S \propto n^{-2/D}$ in degenerate regimes (e.g. $|S| \leq 150 \mu\text{VK}^{-1}$). Applying this approach to SrTiO₃, few-layer Bi₂O₂Se and Pb_{1-x}Sn_xTe uncovers temperature-, doping- and alloy-induced crossovers between three-dimensional and lower-dimensional transport. The method offers a rapid, scattering independent framework to design quantum and thermoelectric properties.

Low-dimensional materials have ascended to the forefront of materials science by virtue of their extraordinary electronic band structures, which can confer dramatically enhanced properties relative to their bulk analogs¹⁻⁴. The reduction in dimensionality, from three-dimensional (3D) to two-dimensional (2D), one-dimensional (1D), or even intermediate confined regimes, fundamentally reshapes the density of states (DOS) through quantum confinement, thereby endowing materials with distinctive electronic, optical, and mechanical characteristics⁵. Such advantages hold particular promise for next-generation electronic devices⁶, sensors⁷, and energy conversion technologies⁸, where performance breakthroughs hinge upon fine control of carrier dynamics at the nanoscale.

A rich array of low-dimensional systems illustrates the transformative impact of reduced dimensionality. For instance, transition metal dichalcogenides (TMDs), such as monolayer Molybdenum disulfide (MoS₂) feature direct bandgaps and pronounced excitonic effects, rendering them ideal platforms for high-efficiency optoelectronics⁹. Likewise, few-layer black phosphorus combines high carrier mobility

with in-plane anisotropy, enabling its integration in advanced electronic and photonic architectures¹⁰. Even in ostensibly 3D materials, such as strontium titanate (SrTiO₃), quantum confinement in thin-film or interfacial configurations drives emergent 2D transport behavior^{11,12}, underscoring the pervasiveness of dimensional tuning across diverse material families. In all these cases, reduced dimensionality amplifies quantum confinement and electron–electron correlations^{13,14}, enabling an unprecedented level of control over material properties. Importantly, the inherent quantum confinement in low-dimensional materials could modify the DOS near band edges, thereby altering carrier mobilities, electrical conductivities, and thermoelectric (TE) properties.

Despite the potential of dimension-driven tuning for engineering high-performance materials, reliably determining the effective dimensionality of the electronic band structure in low-dimensional materials remains nontrivial⁴. Traditional characterization techniques, such as angle-resolved photoemission spectroscopy (ARPES)^{15,16} and scanning tunneling microscopy (STM)^{17,18} have been employed to probe electronic structures. However, these methods often require

¹State Key Laboratory of Functional Crystals and Devices, Fujian Institute of Research on the Structure of Matter, Chinese Academy of Sciences, Fuzhou, Fujian, P.R. China. ²Fujian Science & Technology Innovation Laboratory for Optoelectronic Information of China, Fuzhou, Fujian, P.R. China. ³Department of Materials Science and Engineering, Northwestern University, Evanston, IL, USA. ⁴Fujian College, University of Chinese Academy of Sciences, Fujian, Fuzhou, P.R. China. ⁵University of Chinese Academy of Sciences, Beijing, P.R. China. e-mail: jeff.snyder@northwestern.edu; linyue@fjirsm.ac.cn

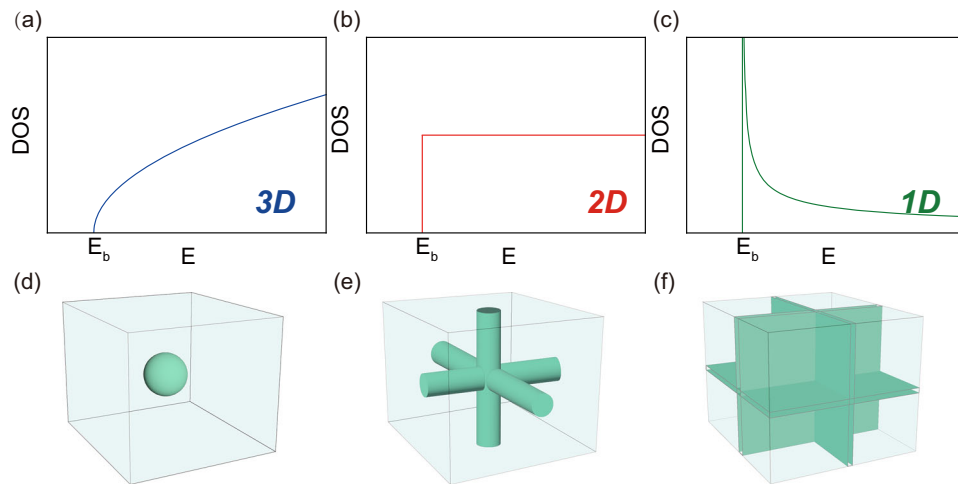


Fig. 1 | Overview of the electronic density of states (top row) and corresponding Fermi surfaces (bottom row) for different dimensional systems. In the top row, the DOS is shown for a **3D**, **2D**, and **1D** materials, illustrating how it evolves with

energy near the band edge E_b . The bottom row depicts the respective Fermi surfaces: **d** 3D (spherical), **e** 2D (cylindrical), and **f** 1D (planar or flat sheet).

complex instrumentation, operate under ultra-high vacuum conditions, and demand pristine surface quality, such as atomic-level smoothness¹⁹. This has motivated the pursuit of transport-based approaches that can probe electronic dimensionality under more accessible experimental conditions.

Typically, the analysis of Seebeck coefficient S and electrical conductivity σ involves both electron scattering and electronic structure considerations. Conductivity is strongly influenced by scattering mechanisms, whereas the Seebeck coefficient predominantly reflects the entropy per charge carrier—a thermodynamic quantity directly related to electronic dimensionality through the DOS²⁰. However, clearly separating these two contributions is inherently ambiguous, often leading to reliance on assumptions about scattering and electronic structure that rarely align exactly with experimental conditions.

In this work, we introduce a broadly applicable strategy to discern the effective electronic dimensionality independently of any assumptions regarding scattering mechanisms. Our approach leverages systematic measurements of Seebeck coefficient S , electrical conductivity σ , and carrier concentration n . By adapting a weighted mobility model^{21–23}, we examine how dimensional confinement modifies the electronic transport behavior. Interestingly, our results show that doping, temperature T , and alloying can trigger transitions between 3D-like and lower dimensional-like behavior in various materials. This framework accelerates the design of systems with tailor-made electronic and TE properties for advanced technological applications.

Results

Simplified model development

Low-dimensional materials (1D, 2D) exhibit electronic properties that deviate markedly from those of conventional 3D semiconductors, primarily because of the dimensional dependence of the DOS. This dependence, in turn, governs carrier dynamics, optical transitions, and transport. Figure 1 presents the generic form of the DOS for 3D, 2D, and 1D systems.

Many 3D semiconductors with roughly spherical Fermi surfaces feature a DOS, $g_{3D}(E)$, that scales with the square root of energy E and vanishes at the Fermi level²⁴ (Fig. 1a). Mathematically,

$$g_{3D}(E) = \frac{(2m^*)^{3/2}}{2\pi^2\hbar^3} \sqrt{E} \quad (1)$$

Where m^* is the effective mass of charge carriers, \hbar is the reduced Planck constant.

In 2D materials, the Fermi surface usually adopts a cylindrical shape. The DOS in this case is constant and independent of energy, reflecting the reduced dimensionality (Fig. 1b):

$$g_{2D}(E) = \frac{1}{a} \cdot \frac{m^*}{\pi\hbar^2} \quad (2)$$

Here, a represents the confinement width perpendicular to the 2D plane. The constant DOS implies a uniform availability of electronic states at different energies near the Fermi level. This constant DOS leads to unique electronic and optical properties that underpin cutting-edge applications in 2D semiconductor quantum wells²⁵ and TMDs⁹.

In 1D systems, including nanowires and carbon nanotubes, the DOS exhibits a characteristic divergence (i.e., a van Hove singularity²⁶) near the band edge (Fig. 1c)

$$g_{1D}(E) = \left(\frac{1}{a}\right)^2 \cdot \frac{1}{\pi\hbar} \sqrt{\frac{2m^*}{E}} \quad (3)$$

where the factor $(\frac{1}{a})^2$ reflects confinement in two perpendicular directions. This divergence means that minor energy shifts can dramatically change the carrier density, a hallmark of reduced dimensionality exploited in sensitive optoelectronic devices^{27–31}.

Because the DOS changes with dimensionality, the carrier concentration n defined by $n = \int_0^\infty g(E)f(E)dE$ also exhibits unique dependencies on the position of the Fermi level E_F . Here, $f(E) = \frac{1}{1 + e^{\frac{E-E_F}{k_B T}}}$ represents the Fermi-Dirac distribution function, where k_B is the Boltzmann constant. These are captured by the following expressions (see Supplementary Information 1.1 for more details):

$$n_{3D} = \frac{(2m_{3D}^*k_B T)^{3/2}}{2\pi^2\hbar^3} F_{\frac{1}{2}}(\eta) \quad (4)$$

$$n_{2D} = \frac{1}{a} \cdot \frac{m_{2D}^*k_B T}{\pi\hbar^2} F_0(\eta) \quad (5)$$

$$n_{1D} = \left(\frac{1}{a}\right)^2 \cdot \frac{(2m_{1D}^*k_B T)^{1/2}}{\pi\hbar} F_{-\frac{1}{2}}(\eta) \quad (6)$$

Here, the reduced Fermi-level $\eta = \frac{E_F}{k_B T}$, and $F_i(\eta)$ is the Fermi-Dirac integral with the reduced energy $\varepsilon = \frac{E}{k_B T}$.

$$F_i(\eta) = \frac{\varepsilon^i}{1 + e^{\varepsilon - \eta}} d\varepsilon \quad (7)$$

These integrals encapsulate how the occupancy of electronic states evolves as a function of T and Fermi-level position. Consequently, the distinct DOS in 3D, 2D, and 1D systems yields different carrier concentration profiles as a function of η .

Boltzmann transport theory, within the relaxation-time approximation, provides a powerful framework for analyzing TE and electronic transport properties in materials of various dimensionalities. Under this approach, the Seebeck coefficient S and electrical conductivity σ can be expressed in terms of the reduced Fermi level η , and the scattering exponent s (or confining dimension a in 2D/1D)²². Specifically,

$$S = \frac{k_B}{e} \left[\frac{(s+1)F_s(\eta)}{sF_{s-1}(\eta)} - \eta \right] \quad (8)$$

$$\sigma = \sigma_{E_0}(T) \cdot sF_{s-1}(\eta) \quad (9)$$

Here, $\sigma_{E_0}(T)$ is a temperature-dependent factor related to the intrinsic material properties and varies with the dimensionality of the system, s is a parameter corresponding to the system's dimensionality and scattering mechanism (see Supplementary Information 1.3 and 1.4 for more details), and the Fermi-Dirac integral $F_{s-1}(\eta)$ incorporates the energy distribution of carriers.

A practical transport toolkit can be built by exploiting the distinct fingerprints that dimensionality D and scattering physics leave on the Seebeck coefficient S in two complementary regimes.

In the non-degenerate regime ($\eta < 0$, practically $\eta \leq -1$), the Pisarenko slope of $S - n$ relation is universal ($-\frac{k_B}{e}$) thus independent of scattering and dimensionality, whereas the intercept retains dependence on the scattering parameter r and D through s (See Section 2.2 and Equation S43 of the Supplementary Information for detail). Consequently, for 1D, 2D, and 3D systems, alike, $S \propto \ln(n^{-1})$, the $S - n$ curve therefore cannot discriminate dimensionality. Instead, the temperature dependence is decisive (see Supplementary Information 2.2 for detail):

$$S(T) \propto \frac{D}{2} \ln T \text{ (e.g. } |S| \geq 200 \mu\text{V K}^{-1}) \quad (10)$$

A single $S(T)$ sweep thus serves as a thermometer for D .

In the degenerate regime ($\eta > 0$, practically $\eta \geq 1$), S acquires a strong carrier-density signature that does resolve dimensionality (see Supplementary Information 2.1 for detail):

$$S(n) \propto n^{-2/D} \text{ (e.g. } |S| \leq 150 \mu\text{V K}^{-1}) \quad (11)$$

Traditional Pisarenko plots measured at a fixed temperature therefore reveal D directly from the power-law exponent. Conversely, in the degenerate regime the Seebeck coefficient S scales linearly with temperature T for every dimensionality, so an $S - T$ plot offers no leverage for distinguishing D , but differ depending on the scattering.

In this work, we adopt a curve-wise m^* assumption within the effective-mass framework^{32,33}. For each $S - n$ data set at fixed T (or $S - T$ at fixed n), we fit with a single m^* that captures the local band curvature and serves as a transport descriptor. When a single m^* fails to reconcile the data with the D -dimensional Pisarenko relation, the systematic deviation is interpreted as evidence of non-parabolicity, band modification (e.g., convergence or inversion), or a change in the effective D . Importantly, our inference of D relies on the scaling

Table 1 | The carrier concentration n and temperature T dependency of Seebeck coefficient S , and transport exponent s for various carrier scattering mechanisms in 1D, 2D, and 3D systems

Scattering mechanisms	Dimensionality	$S - n$ ($\eta \gg -1$)	$S - T$ ($\eta \ll -1$)	s
Acoustic Phonon or Non-Polar Optical Phonon	3D	$n^{-2/3}$	$\frac{3}{2} \ln(T)$	1
	2D	n^{-1}	$\ln(T)$	
	1D	n^{-2}	$\frac{1}{2} \ln(T)$	
Ionized Impurity	3D	$n^{-2/3}$	$\frac{3}{2} \ln(T)$	3
	2D	n^{-1}	$\ln(T)$	5/2
	1D	n^{-2}	$\frac{1}{2} \ln(T)$	2
Piezoelectric or Polar Optical Phonon	3D	$n^{-2/3}$	$\frac{3}{2} \ln(T)$	2
	2D	n^{-1}	$\ln(T)$	3/2
	1D	n^{-2}	$\frac{1}{2} \ln(T)$	1

Note: the scattering exponent (commonly denoted r) encodes the underlying scattering mechanism (See Section 1.2 of the Supplementary Information for detail). Of particular relevance is the relationship $s = r + \frac{D}{2}$, where D is dictated by dimensionality, taking values of 1 for 1D systems, 2 for 2D systems, and 3 for 3D systems (see Section 1.3 of the Supplementary Information for a detailed derivation). Consequently, changing r directly shifts the transport exponent s .

exponent of S vs n , which is insensitive to the absolute magnitude of m^* (i.e., m^* sets the prefactor, not the exponent).

Carrier scattering mechanisms, such as acoustic phonon, ionized impurity, piezoelectric, or polar optical phonon scattering, impose unique dependencies on carrier energy and temperature^{31,34-36}. Once the dominant mechanism is established, the associated transport exponent s may become an independent fingerprint of dimensionality. For example, for ionized-impurity and polar-optical-phonon scattering, each effective DOS dimensionality D maps onto a unique s value (Table 1). Experimentally, s can be extracted by measuring the Seebeck coefficient S and electrical conductivity σ while systematically tuning the carrier concentration at a fixed temperature, then fitting the joint $S - \sigma$ response. The resulting s can be matched to the theoretical $s(D)$ catalogue (Table 1), providing a rapid, self-consistent check on the dimensionality already inferred from $S(T)$ or Pisarenko $S(n)$ analysis. (A detailed explanation can be found in the Introduction of Section 2 and in Section 2.1 of the Supplementary Information.)

Combining these measurements allows one to establish the effective DOS dimensionality in a range of low-dimensional or nanostructured systems.

Case Studies

Using our transport model framework, we next analyze representative low-dimensional systems to illustrate how their electronic dimensionality and dominant scattering mechanisms are revealed.

Dimensional crossover from 3D- to 2D-like transport in heavily doped SrTiO₃. A cross-analysis of six independent data sets^{11,37-41}

(Fig. 2) exposes a universal dimensional crossover in SrTiO₃ that is triggered once the carrier density surpasses $n \approx 1 \times 10^{20} \text{ cm}^{-3}$. Below this threshold, the transport is well described by a conventional 3D DOS. The Seebeck coefficient varies with temperature as $3/2 \ln T$ and the Pisarenko relation follows the canonical $S \propto n^{-2/3}$ dependence. As the carrier density rises beyond this threshold, both signatures evolve in concert toward the behaviour expected for a 2D DOS. Specifically, the logarithmic prefactor in $S(T)$ collapses to unity, yielding $S \propto \ln T$, while the slope of the $S - n$ curve steepens to $S \propto n^{-1}$ (the detailed calculation procedure is described in Supplementary Information 3.1 and illustrated in Figs. S1 to S3).

Taken together, these observations argue that heavily doped SrTiO₃ develops a Fermi surface that is effectively 2D, in line with

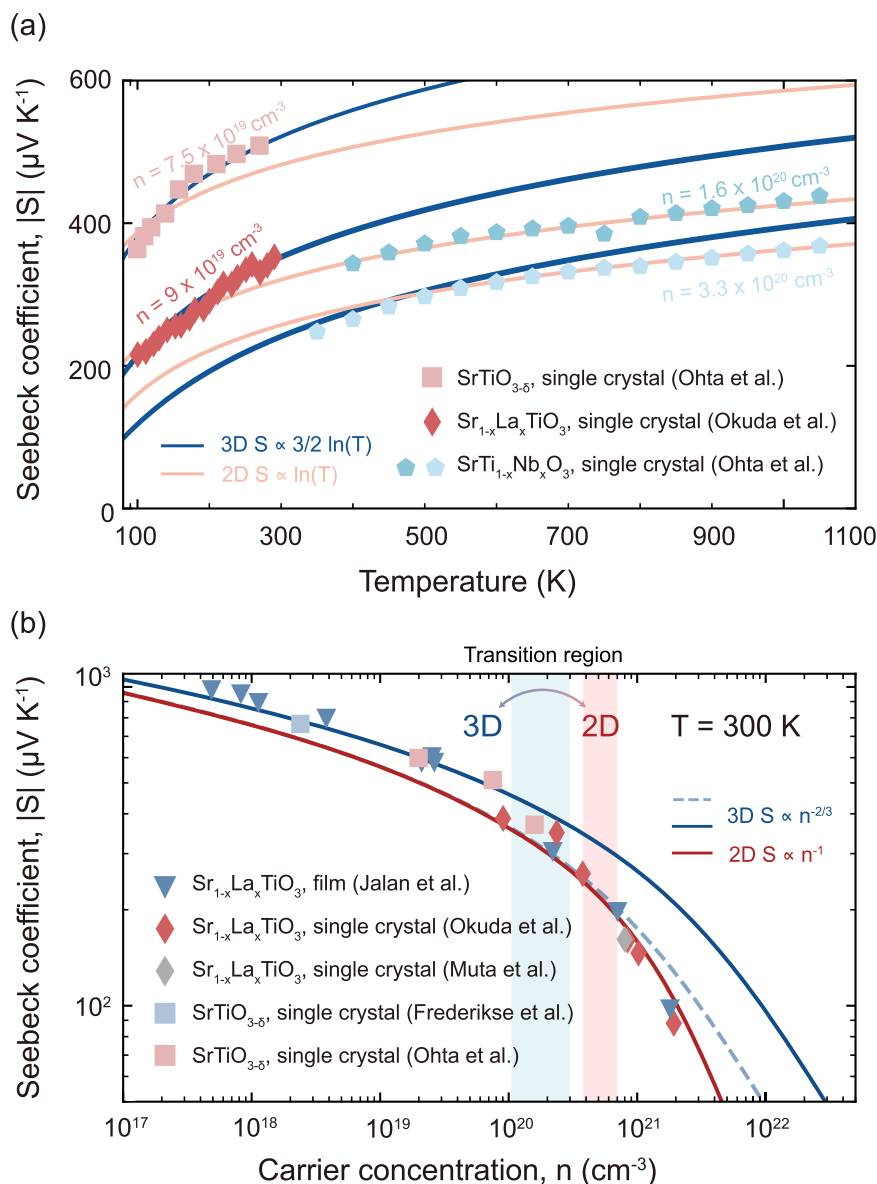


Fig. 2 | Thermoelectric transport fingerprints of n-type SrTiO₃. Data are compiled from La doped, Nb doped and oxygen deficient crystals and films in Refs. 11,37–41. a Temperature evolution of S for oxygen deficient, La and Nb doped crystals. At low n , the data clearly follow $3/2 \ln T$ characteristic of 3D DOS while at high n above 10^{20} cm^{-3} the data follow $\ln T$ characteristic of a 2D DOS; datasets that

straddle the crossover concentration reproduce the change in slope expected for reduced dimensionality. **b** Room temperature S versus Hall carrier concentration n . At high n the data clearly follow the 2D DOS prediction (red curve) as opposed to the 3D (blue curve); the inflection at $n \approx 1 \times 10^{20} \text{ cm}^{-3}$ signals entry into the 2D regime.

recent DFT predictions of flattened t_{2g} sub bands under strong filling⁴². This quasi-2D behavior arises from orbital-selective hybridization: in-plane Ti-d_{xy} and O-p coupling yields dispersive bands, whereas out-of-plane (z) hybridization is symmetry-suppressed, producing weak dispersion and cylindrical Fermi-surface sections. The result cautions that bulk SrTiO₃ cannot always be treated within a simple 3D parabolic band picture once carrier densities approach 10^{20} cm^{-3} , and it underscores how modest chemical doping can unlock low dimensional transport physics without artificial confinement.

Temperature-triggered transition from 1D-like to 3D-like transport in few-layer bismuth oxyarsenide (Bi₂O₂Se). Bismuth Oxyarsenide (Bi₂O₂Se) features a layered crystal structure consisting of alternating [Bi₂O₂]_n²ⁿ⁺ layers and [Se]_n²ⁿ⁻ layers, held together by weak electrostatic interactions⁴³. Recent studies by Yang et al. have investigated the carrier scattering mechanisms in Bi₂O₂Se flakes to be polar optical

phonon/piezoelectric scattering mechanisms and their impact on TE performance⁴⁴.

In this study, our model uncovers that the electron transport behavior undergoes dimensional evolution. As the T increases, transport behavior transitions from a 1D to higher-dimensional regime. This transition is discovered by analyzing the relationship between S and n (detailed calculation procedures can be found in Supplementary Information 3.2, along with Figs. S4 and S5). At 60 K, a 1D transport model fits the $S - n$ data (Fig. 3b), whereas at 100 K, a 2D model is more appropriate (Fig. 3c). By 300 K, a 3D model best describes the $S - n$ relationship (Fig. 3d). The change in transport exponent s further confirmed this transition. The $S - \sigma$ relationship follows the $s=1$ relation at 60 K, $s=1.5$ at 100 K, and $s=2$ at 300 K. Assuming optical phonon/piezoelectric scattering mechanism throughout, this observation indicates that the transport behaviour shifts from 1D to 3D as T increases (Table 1). This effect may originate from its layered crystal/electronic anisotropy: weak interlayer coupling along the out-of-plane

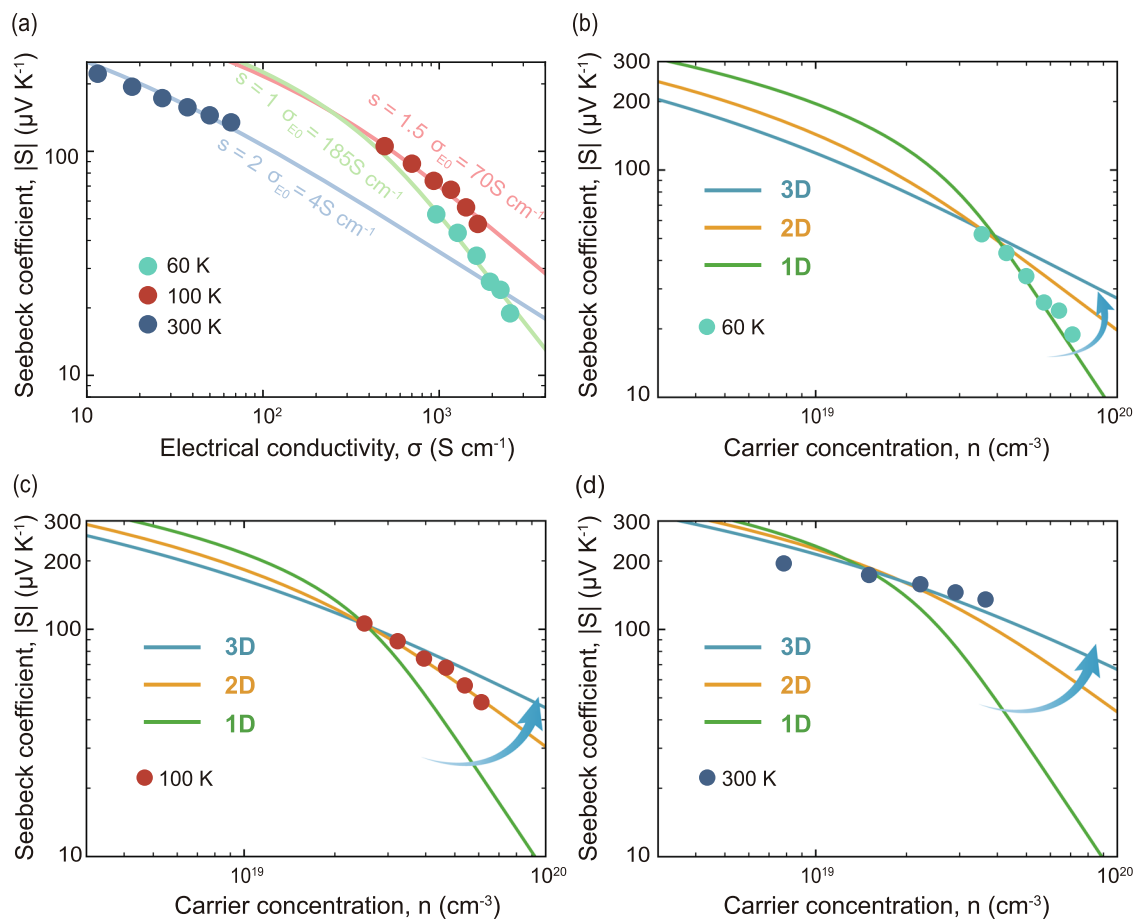


Fig. 3 | Temperature-dependent evolution of carrier transport behavior in Few-layer $\text{Bi}_2\text{O}_2\text{Se}$, data adapted from Yang et al.⁴⁴. a $S - \sigma$ data for gate voltages of 10–60 V, showing the temperature dependence of the exponent s at different

temperatures: $s = 1$ at 60 K, $s = 1.5$ at 100 K, and $s = 2$ at 300 K. **b–d** Relationship between carrier concentration and the Seebeck coefficient at 60 K (**b**), 100 K (**c**), and 300 K (**d**).

direction produces a highly anisotropic Fermi surface and effective mass (nearly isotropic in-plane but elongated along k_z)⁴⁵. At low temperature, suppressed interlayer hopping confines carriers within the layers, yielding quasi-1D-like scaling; with increasing T , phonon-assisted interlayer transport progressively activates transverse conduction, driving a 1D \rightarrow 2D \rightarrow 3D evolution. These temperature-induced dimensional transitions expand our understanding of carrier dynamics in $\text{Bi}_2\text{O}_2\text{Se}$ and highlight novel routes for property optimization.

Topological phase transition and emergent 1D-like transport in $\text{Pb}_{1-x}\text{Sn}_x\text{Te}$ alloy. Topological insulators (TIs) represent a unique class of quantum materials, characterized by metallic surface states coupled with insulating bulk electronic structures^{46,47}. These properties offer significant promise for applications in next-generation electronic devices⁴⁸. Remarkably, many TIs, particularly Bi_2Te_3 -based alloys, also exhibit outstanding TE performance and are widely employed in commercial TE technologies⁴⁹. Recent studies suggest that bulk electronic structures in TIs can induce novel TE behaviors. In particular, band inversion and the associated band warping in TIs can increase valley degeneracy and effective carrier pocket multiplicity^{50,51}, enhancing the Seebeck coefficient S and power factor $S^2\sigma$. Despite these promising insights, transport phenomena originating within the bulk states of TIs remain relatively understudied, especially in the context of unconventional TE effects driven by topological electronic structure transitions in the bulk electronic structure.

Here, we investigate the transport behavior across the topological phase transition in $\text{Pb}_{1-x}\text{Sn}_x\text{Te}$, using our generalized transport model, supported by both previously reported data^{52–60} and systematic

experiments performed in this work (further experimental details are provided in Method section). This alloy system spans from the normal insulator PbTe (trivial band ordering) to the topological crystalline insulator SnTe (inverted bands), providing an ideal platform to study how TE properties evolve with changes in band topology. As the alloy approaches a critical composition ($x_c \approx 0.6$), we observe a striking deviation from ordinary 3D transport toward a 1D-like transport regime (Fig. 4a). In compositions well away from x_c , the S versus n follows the expected 3D trend $S \propto n^{-2/3}$ even as the effective mass (m^*/m_e) varies with alloying (Fig. 4b). Near the critical point, however, the $S - n$ relationship steepens to $S \propto n^{-2}$, closely resembling 1D transport behavior and clearly deviating from the 3D model (Fig. 4a). This motivates fitting with the 1D transport model, from which a self-consistent (curve-wise constant) 1D m^* is extracted. This dimensional crossover is accompanied by a dramatic drop in the apparent effective mass: at $x \approx 0.6$, m^*/m_e is roughly three orders of magnitude lower than in the 3D regime (Fig. 4b) (further calculation details are provided in Supplementary Information 3.3 and Fig. S6). Such an abrupt reduction in m^*/m_e is consistent with the emergence of massless or light Dirac-like carriers at the topological transition⁶¹. This behavior supports, rather than contradicts, the conclusion that transport channels exhibit 1D-like characteristics in the vicinity of the topological transition.

At the critical composition, the bulk band gap of $\text{Pb}_{1-x}\text{Sn}_x\text{Te}$ narrows to zero and band inversion occurs at the L-points of the Brillouin zone, resulting in the formation of linear Dirac cones (a hallmark of the topological phase transition)^{50,61}. This inversion marks the point where the alloy's electronic structure is reorganized from normal to

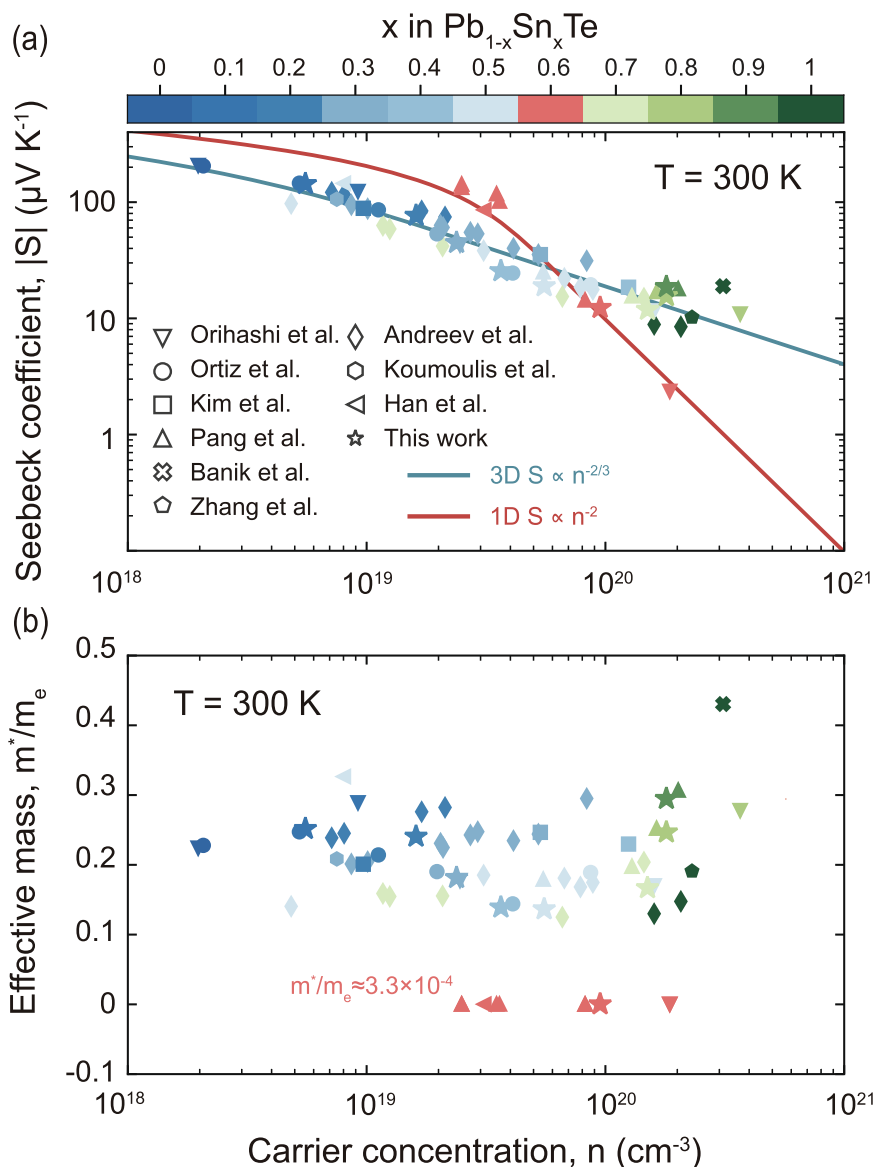


Fig. 4 | Topological phase transition of in $\text{Pb}_{1-x}\text{Sn}_x\text{Te}$ alloys. **a** Relationship between S and n at $T = 300\text{ K}$, compiled from Refs. 52–60. At the critical composition $x_c \approx 0.6$, the alloy exhibits unexpected 1D-like transport behavior ($S \propto n^{-2}$), distinctly deviating from the typical 3D transport characterized by $S \propto n^{-2/3}$.

b Effective mass (m^*/m_e) as a function of n , highlighting a dramatic decrease (approximately three orders of magnitude) in effective mass precisely at the critical composition.

topological. We hypothesize that the unusual 1D-like transport observed in the bulk $\text{Pb}_{0.4}\text{Sn}_{0.6}\text{Te}$ at this transition originates from topologically derived conducting channels that effectively reduce the dimensionality of charge transport. In other words, as the system's bulk bands invert, new conducting states associated with the topological phase boundary can arise and carry current in a lower-dimensional manner than the 3D bulk.

One plausible scenario is the appearance of topologically protected boundary or edge states along internal interfaces or defects. For instance, microscopic regions of trivial and inverted band order may coexist near the transition (due to alloy fluctuations or strain), and the interfaces between these regions would host 2D topological surface states⁶². If these interfaces percolate or form networks, charge carriers might preferentially flow along them. In extreme cases, e.g. along line defects or along the intersection of facets, these percolating pathways could behave like quasi-1D conductors embedded in the 3D material^{63,64}. This provides a reasonable explanation for the 1D-like $S \propto n^{-2}$ scaling: the transport is dominated by carriers confined to

filamentary or stripe-like topological conductive paths, rather than the bulk 3D conduction band. Notably, analogous phenomena have been reported in other topological systems, lending credence to our interpretation. Bismuth antimony alloys ($\text{Bi}_{1-x}\text{Sb}_x$) undergo a well-known topological band inversion; remarkably, theory and experiments have shown that in the inverted regime, crystal dislocations can host 1D helical modes that conduct along the dislocation line in the bulk crystal⁶⁵. These 1D topological defect states (predicted in weak TIs) effectively act as internal wires with quantum-protected transport, and they have indeed been suggested to contribute to the electrical conduction in $\text{Bi}_{1-x}\text{Sb}_x$ crystals near the topological transition. Likewise, elemental bismuth, recently identified as a higher-order topological insulator, features conducting hinge states 1D channels running along the edges where crystal faces meet⁶⁶. These topological hinge modes allow electrons in Bi to travel ballistically along the crystal edges, which helps explain Bi's unusually long carrier mean free path and ability to conduct with very low carrier densities. The existence of such 1D conduction pathways in nominally 3D topological materials

underscores that dimensionality of transport can be intrinsically altered by topology.

By analogy, we suggest that in $\text{Pb}_{1-x}\text{Sn}_x\text{Te}$, the closing of the bulk gap and onset of band inversion create conditions for 1D-like transport channels. These may arise from topology-enabled line, hinge, or interface modes, or from percolating networks of locally inverted and trivial regions that can dominate conduction at the critical composition x_c . Importantly, the 3D to 1D scaling appears not only in polycrystals studied but also in single-crystal datasets near x_c (e.g., Orihashi et al.⁵⁵), indicating that the effect does not rely on macroscopic crystallinity. Microstructure chiefly modulates the density and connectivity of these pathways, and thus the amplitude of the 1D-like signature, but is not required for their existence; high-quality single crystals may suppress extrinsic networks yet still exhibit intrinsic 1D-like scaling in the vicinity of x_c .

Crucially, the emergence of these 1D-like pathways at x_c offers a direct performance benefit: the effective transport dimensionality reduction leads to an enhanced Seebeck coefficient at a given carrier concentration (since S in a 1D-like system can achieve larger values than in 3D, for comparable n below $6 \times 10^{19} \text{ cm}^{-3}$) (Fig. 4a). In tandem with the ultralow effective mass of the Dirac-like bulk carriers, this drives a marked improvement in the TE quality factors. Indeed, compositions near $x \approx 0.6$ are observed to exhibit significantly boosted TE performance⁵².

We propose that this enhancement originates from the topologically driven changes in the electronic structure; essentially, the material taps into high-mobility, low-dimensional transport channels at the transition.

This finding not only deepens our understanding of how topological phase transitions can influence bulk transport properties but also suggests a novel strategy for engineering superior TEs. By tuning a material to the brink of a topological phase change (through alloying, strain, or other means), one can invoke these protected, high-conductivity 1D-like pathways and achieve an optimal combination of high Seebeck coefficient and mobility.

In summary, the $\text{Pb}_{1-x}\text{Sn}_x\text{Te}$ alloy at its critical composition $x_c \approx 0.6$ demonstrates an intrinsic quasi-1D transport mode arising from a topological electronic transition. This discovery opens new avenues for exploiting topological transitions as a tool for designing TE materials, potentially guiding the development of next-generation TE materials with unprecedented performance through the controlled dimensionality of electronic transport.

Assessing electronic dimensionality in organic semiconductors: PBTTT as a model system. Despite the well-known practical difficulty of obtaining reliable Hall carrier densities in organic conductors^{67,68}, we assessed the applicability of our framework using the extensively studied Poly[2,5-bis(3-dodecylthiophen-2-yl)thieno[3,2-b]thiophene] (PBTTT) as a model system. We analyzed a few literature datasets^{69–72} that report both S and n (Fig. 5). PBTTT shows a scattering evolution from $s=3$ to $s=1$ with increasing doping^{69–71} (Fig. 5a), implying a transition toward acoustic-phonon dominated transport²² and compatible with coherent, quasi-2D metallic behavior^{73,74} at high conductivity ($\sigma \geq 200 \text{ Scm}^{-1}$).

At the single-study level, some datasets (e.g., Chen^{69,70} (Fig. 5c, e) and Kang⁷¹ (Fig. 5d)) exhibit strong 2D-like trends, whereas others (e.g., Wang⁷² (Fig. 5f)) appear 3D-like. To mitigate dataset-specific Hall uncertainties, we pooled all points at 300 K (Fig. 5b). The aggregated data largely occupy the overlap region between our 3D- and 2D-discriminative bands, so we cannot claim a universal 2D assignment for PBTTT at high doping.

We infer that the apparent dimensionality in organics is highly sensitive to disorder, such as set by intrinsic microstructure, dopant distribution, and processing history (e.g., crosslinking), as highlighted in prior studies^{75–78}. Establishing dimensionality robustly in

organics will therefore benefit from independent carrier-density benchmarks (e.g., coulometry, IR sum-rules, or gate-capacitance areal densities) and cross-checks with microscopic probes where available.

Discussion

We introduced a simple yet powerful transport framework for diagnosing electronic dimensionality in semiconductors from standard measurements (S , σ , n). Applied to SrTiO_3 , $\text{Bi}_2\text{O}_2\text{Se}$ and $\text{Pb}_{1-x}\text{Sn}_x\text{Te}$, the analysis captures 1D/2D-like to 3D crossovers driven by doping, temperature, and alloying, linking macroscopic transport to low-dimensional electronic structure.

The method can operate directly on published datasets and open repositories (e.g., StarryData2), enabling broad screening for dimensionality signatures. It is complementary to microscopic probes, such as ARPES, quantum oscillations, and first-principles calculations, which can validate the inferred D and scattering. The framework is agnostic to chemistry and extends naturally to other semiconductors and layered materials.

To remain tractable, we adopt standard assumptions: relaxation-time approximation with power-law scattering, a single dominant band, and a curve-wise constant m^* . These can be strained in narrow-gap or strongly anisotropic systems, in multi-band regimes, or where strong correlations/disorder dominate.

Future work may (i) incorporate multi-band formulations; (ii) treat anisotropic effective-mass tensors and beyond-power-law energy-dependent scattering; and (iii) integrate high-throughput computation and machine-learning over large databases to identify materials with unconventional dimensional transport. Beyond inorganic systems, the same logic can be adapted to organic TEs, providing a unified perspective on dimensional transport across diverse material classes.

Overall, the framework deepens understanding of carrier dynamics and offers practical guidance for designing next-generation TEs and electronic materials, where controlling dimensionality can unlock enhanced performance.

Methods

Theoretical analysis

A simplified transport model was established to describe the dependence of the Seebeck coefficient on temperature $S(T)$ or carrier concentration $S(n)$ across different electronic dimensionalities. The model assumes a single dominant band and employs the relaxation-time approximation with power-law scattering. Full derivations and parameter details are provided in the Supplementary Information.

Materials synthesis

Samples with nominal compositions of $\text{Pb}_{1-x}\text{Sn}_x\text{Te}$ ($x=0.1–0.9$, $\Delta x=0.1$) were synthesized using high-purity Pb, Sn, and Te elements. Stoichiometric mixtures, each weighing approximately 8 g, were loaded into quartz tubes, evacuated to a residual pressure of 10^{-4} mbar, and sealed. The sealed tubes were then heated gradually to 1100°C over 11 h, maintained at this temperature for 12 h to ensure complete melting and homogeneity, cooled to 900°C over 2 h, held at this intermediate temperature for 6 h to facilitate phase stabilization, and subsequently furnace-cooled to room temperature.

The resulting ingots were mechanically ground into fine powders using ball milling. The powders were then densified via spark plasma sintering (SPS) at 500°C for 5 min under an axial compressive pressure of 40 MPa in vacuum, producing high-density, polycrystalline bulk samples.

Transport measurements

Electrical conductivity and Hall coefficient measurements were performed using the standard 4-point Van der Pauw method under a

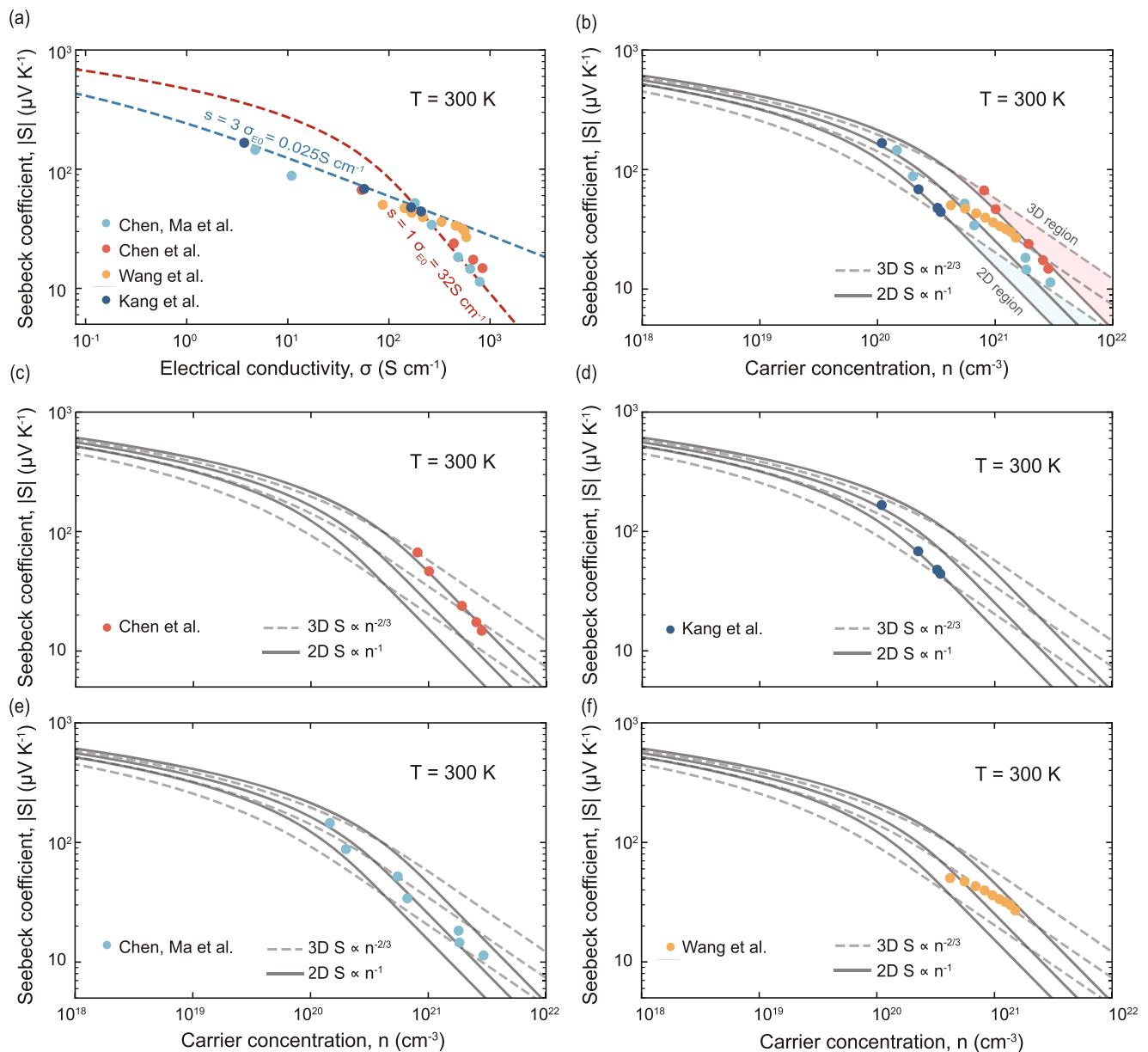


Fig. 5 | Thermoelectric properties of PBTTT at 300 K. Data compiled from Chen, Ma et al.⁶⁹, Chen et al.⁷⁰, Wang et al.⁷², and Kang et al.⁷¹. **a** $S - \sigma$ relation at 300 K. The slopes indicate an evolution of the scattering descriptor from $s = 3$ at low conductivity toward $s = 1$ at high conductivity. **b** $S - n$ relation at 300 K for the aggregated dataset. Reference curves show the degenerate Pisarenko scalings for 3D ($S \propto n^{-2/3}$) and 2D ($S \propto n^{-1}$); the shaded band marks the region where $S - n$

discriminates dimensionality (red for 3D, and blue for 2D). Most points fall in the 3D/2D overlap, so a universal 2D assignment for PBTTT at 300 K cannot be made. Differences likely reflect variations in microstructure/disorder, dopant distribution, and processing. **c-f** $S - n$ plotted separately for Chen et al., Kang et al., Chen, Ma et al., and Wang et al., using the same reference curves. Some individual datasets lean 2D-like at high doping, whereas others appear more 3D-like.

0.8 T magnetic field in a high-vacuum environment⁷⁹. The Seebeck coefficients were measured by establishing a temperature gradient of approximately ± 5 K across the sample, employing chromel-Nb thermocouples for accurate temperature detection⁸⁰.

Reporting summary

Further information on research design is available in the Nature Portfolio Reporting Summary linked to this article.

Data availability

All data supporting the findings of this study are available within the paper and its Supplementary Information. Source data are publicly available on Figshare at <https://doi.org/10.6084/m9.figshare.30230689>. Source data are provided with this paper.

Code availability

Customized Python scripts used in this study are available at Code Ocean: <https://doi.org/10.24433/CO.1401080.v1>. All analyses were performed using Python 3.8.5.

References

1. Zhao Y. et al. Low-symmetry PdSe₂ for high performance thermoelectric applications. *Adv. Funct. Mater.* **30**, 2004896 (2020).
2. Lee, S. et al. Anisotropic in-plane thermal conductivity of black phosphorus nanoribbons at temperatures higher than 100. K. *Nat. Commun.* **6**, 8573 (2015).
3. Fust, S. et al. Quantum-confinement-enhanced thermoelectric properties in modulation-doped GaAs-AlGaAs core-shell nanowires. *Adv. Mater.* **32**, e1905458 (2020).

4. Tayari, V. et al. Quasi-two-dimensional thermoelectricity in SnSe. *Phys. Rev. B* **97**, 045424 (2018).
5. Mao, J., Liu, Z. & Ren, Z. Size effect in thermoelectric materials. *npj Quantum Mater.* **1**, 1–9 (2016).
6. Wu, P. et al. Next-generation machine vision systems incorporating two-dimensional materials: progress and perspectives. *InfoMat* **4**, e12275 (2022).
7. Yang, Q. et al. Controlled optoelectronic response in van der Waals heterostructures for in-sensor computing. *Adv. Funct. Mater.* **32**, 202207290 (2022).
8. Kanahashi, K., Pu, J. & Takenobu, T. 2D materials for large-area flexible thermoelectric devices. *Adv. Energy Mater.* **10**, 1902842 (2020).
9. Wang, Q. H., Kalantar-Zadeh, K., Kis, A., Coleman, J. N. & Strano, M. S. Electronics and optoelectronics of two-dimensional transition metal dichalcogenides. *Nat. Nanotechnol.* **7**, 699–712 (2012).
10. Li, L. et al. Black phosphorus field-effect transistors. *Nat. Nanotechnol.* **9**, 372–377 (2014).
11. Ohta, H. et al. Giant thermoelectric Seebeck coefficient of a two-dimensional electron gas in SrTiO₃. *Nat. Mater.* **6**, 129–134 (2007).
12. Sun J., Singh D. J. Thermoelectric properties of n-type SrTiO₃. *APL Mater.* **4**, 104803 (2016).
13. Choi, W. S., Ohta, H. & Lee, H. N. Thermopower enhancement by fractional layer control in 2D oxide superlattices. *Adv. Mater.* **26**, 6701–6705 (2014).
14. Tan, T., Jiang, X., Wang, C., Yao, B. & Zhang, H. 2D material optoelectronics for information functional device applications: status and challenges. *Adv. Sci. (Weinh.)* **7**, 2000058 (2020).
15. Chen, Y. et al. Experimental realization of a three-dimensional topological insulator, Bi₂Te₃. *Science* **325**, 178–181 (2009).
16. Zhao C. X. et al. Unexpected 18-fold overlapped feathery Fermi pockets in typical thermoelectric Bi_{0.5}Sb_{1.5}Te₃. *Phys. Rev. Lett.* **134**, 086401 (2025).
17. Damascelli, A., Hussain, Z. & Shen, Z.-X. Angle-resolved photoemission studies of the cuprate superconductors. *Rev. Mod. Phys.* **75**, 473 (2003).
18. Binnig, G. & Rohrer, H. Scanning tunneling microscopy. *Surf. Sci.* **126**, 236–244 (1983).
19. King, P. et al. Subband structure of a two-dimensional electron gas formed at the polar surface of the strong spin-orbit perovskite KTaO₃. *Phys. Rev. Lett.* **108**, 117602 (2012).
20. Brown D. R. et al. Phase transition enhanced thermoelectric figure-of-merit in copper chalcogenides. *Apl. Mater.* **1**, 052107 (2013).
21. Kang, S. D., Dylla, M. & Snyder, G. J. Thermopower-conductivity relation for distinguishing transport mechanisms: Polaron hopping in CeO₂ and band conduction in SrTiO₃. *Phys. Rev. B* **97**, 235201 (2018).
22. Kang, S. D. & Snyder, G. J. Charge-transport model for conducting polymers. *Nat. Mater.* **16**, 252–257 (2017).
23. Snyder, G. J. et al. Weighted mobility. *Adv. Mater.* **32**, e2001537 (2020).
24. Brod, M. K. & Snyder, G. J. Orbital chemistry of high valence band convergence and low-dimensional topology in PbTe. *J. Mater. Chem. A* **9**, 12119–12139 (2021).
25. Schmitt-Rink, S., Chemla, D. & Miller, D. A. Linear and nonlinear optical properties of semiconductor quantum wells. *Adv. Phys.* **38**, 89–188 (1989).
26. Van Hove, L. The occurrence of singularities in the elastic frequency distribution of a crystal. *Phys. Rev.* **89**, 1189–1193 (1953).
27. Parker, D., Chen, X. & Singh, D. J. High three-dimensional thermoelectric performance from low-dimensional bands. *Phys. Rev. Lett.* **110**, 146601 (2013).
28. Raseong Kim, S. D. & Mark, S. Lundstrom. Influence of dimensionality on thermoelectric device performance. *J. Appl. Phys.* **105**, 034506 (2009).
29. Hicks, L. D. & Dresselhaus, M. S. Effect of quantum-well structures on the thermoelectric figure of merit. *Phys. Rev. B* **47**, 12727 (1993).
30. Hicks, L. D. & Dresselhaus, M. S. Thermoelectric figure of merit of a one-dimensional conductor. *Phys. Rev. B* **47**, 16631 (1993).
31. Lundstrom, M. Fundamentals of carrier transport, 2nd edn. *Meas. Sci. Technol.* **13**, 230–230 (2002).
32. Snyder, G. J., Pereyra, A. & Gurunathan, R. Effective mass from Seebeck coefficient. *Adv. Funct. Mater.* **32**, 2112772 (2022).
33. Dongmin Kang S., Snyder G. J. Transport property analysis method for thermoelectric materials: Material quality factor and the effective mass model. *arXiv e-prints*, arXiv: 1710.06896 (2017).
34. Fistul' VI. Transport phenomena in heavily doped semiconductors. In: *Heavily doped semiconductors*. (Springer New York, 1969).
35. Bardeen, J. & Shockley, W. Deformation potentials and mobilities in non-polar crystals. *Phys. Rev.* **80**, 72 (1950).
36. Herring, C. & Vogt, E. Transport and deformation-potential theory for many-valley semiconductors with anisotropic scattering. *Phys. Rev.* **101**, 944 (1956).
37. Jalan B., Stemmer S. Large Seebeck coefficients and thermoelectric power factor of La-doped SrTiO₃ thin films. *Appl. Phys. Lett.* **97**, 42106 (2010).
38. Okuda, T., Nakanishi, K., Miyasaka, S. & Tokura, Y. Large thermoelectric response of metallic perovskites: Sr_{1-x}La_xTiO₃ (0 ≤ x ≤ 0.1). *Phys. Rev. B* **63**, 113104 (2001).
39. Frederikse, H., Thurber, W. & Hosler, W. Electronic transport in strontium titanate. *Phys. Rev.* **134**, A442 (1964).
40. Muta, H., Kurosaki, K. & Yamanaka, S. Thermoelectric properties of reduced and La-doped single-crystalline SrTiO₃. *J. Alloy. Compd.* **392**, 306–309 (2005).
41. Ohta S., Nomura T., Ohta H., Koumoto K. High-temperature carrier transport and thermoelectric properties of heavily La- or Nb-doped SrTiO₃ single crystals. *J. Appl. Phys.* **97**, 034106 (2005).
42. Dylla, M. T., Kang, S. D. & Snyder, G. J. Effect of two-dimensional crystal orbitals on Fermi surfaces and electron transport in three-dimensional perovskite oxides. *Angew. Chem.* **131**, 5557–5566 (2019).
43. Cheng, T. et al. Raman spectra and strain effects in bismuth oxychalcogenides. *J. Phys. Chem. C.* **122**, 19970–19980 (2018).
44. Yang, F. et al. Gate-tunable polar optical phonon to piezoelectric scattering in few-layer Bi₂O₂Se for high-performance thermoelectrics. *Adv. Mater.* **33**, e2004786 (2021).
45. Ding, X. et al. Bi₂O₂Se: A rising star for semiconductor devices. *Matter* **5**, 4274–4314 (2022).
46. Moore, J. E. The birth of topological insulators. *Nature* **464**, 194–198 (2010).
47. Anirban, A. 15 years of topological insulators. *Nat. Rev. Phys.* **5**, 267–267 (2023).
48. Breunig, O. & Ando, Y. Opportunities in topological insulator devices. *Nat. Rev. Phys.* **4**, 184–193 (2022).
49. Witting, I. T. et al. The thermoelectric properties of bismuth telluride. *Adv. Electron Mater.* **5**, 1800904 (2019).
50. Toriyama M. Y., Snyder G. J. Topological insulators for thermoelectrics: a perspective from beneath the surface. *Innovation* **6**, 100782 (2025).
51. Toriyama, M. Y. & Snyder, G. J. Are topological insulators promising thermoelectrics? *Mater. Horiz.* **11**, 1188–1198 (2024).
52. Pang, H. et al. Realizing ranged performance in SnTe through integrating bands convergence and DOS distortion. *J. Materiomics* **8**, 184–194 (2022).
53. Ortiz, B. R., Adamczyk, J. M., Gordiz, K., Braden, T. & Toberer, E. S. Towards the high-throughput synthesis of bulk materials: Thermoelectric PbTe–PbSe–SnTe–SnSe alloys. *Mol. Syst. Des. Eng.* **4**, 407–420 (2019).

54. Kim, G., Yun, J. H. & Rhyee, J.-S. Anomalous thermoelectric power and polaronic transport in the vicinity of topological phase transition of $\text{Pb}_{1-x}\text{Sn}_x\text{Te}$. *J. Phys. Chem. Solids* **126**, 11–16 (2019).
55. Orihashi, M., Noda, Y., Chen, L.-D., Goto, T. & Hirai, T. Effect of tin content on thermoelectric properties of p-type lead tin telluride. *J. Phys. Chem. Solids* **61**, 919–923 (2000).
56. Zhang, Q. et al. High thermoelectric performance by resonant dopant indium in nanostructured SnTe. *Proc. Natl Acad. Sci.* **110**, 13261–13266 (2013).
57. Banik, A., Vishal, B., Perumal, S., Datta, R. & Biswas, K. The origin of low thermal conductivity in $\text{Sn}_{1-x}\text{Sb}_x\text{Te}$: phonon scattering via layered intergrowth nanostructures. *Energy Environ. Sci.* **9**, 2011–2019 (2016).
58. Koumoulis, D. et al. Site-specific contributions to the band inversion in a topological crystalline insulator. *Adv. Electron Mater.* **1**, 1500117 (2015).
59. Han, M.-K., Zhou, X., Uher, C., Kim, S.-J. & Kanatzidis, M. G. Increase in the figure of merit by Cd-substitution in $\text{Sn}_{1-x}\text{Sb}_x\text{Te}$ and effect of Pb/Sn ratio on thermoelectric properties. *Adv. Energy Mater.* **2**, 1218–1225 (2012).
60. Andrevv, A. The band edge structure of the IV–VI semiconductors. *Le. J. de Phys. Colloq.* **29**, C4-50–C54-61 (1968).
61. Xiao, Y. et al. Approaching topological insulating states leads to high thermoelectric performance in n-type PbTe. *J. Am. Chem. Soc.* **140**, 13097–13102 (2018).
62. Qi, X.-L. & Zhang, S.-C. Topological insulators and superconductors. *Rev. Mod. Phys.* **83**, 1057–1110 (2011).
63. Langbehn, J., Peng, Y., Trifunovic, L., Von Oppen, F. & Brouwer, P. W. Reflection-symmetric second-order topological insulators and superconductors. *Phys. Rev. Lett.* **119**, 246401 (2017).
64. Lin, C. et al. Visualization of the strain-induced topological phase transition in a quasi-one-dimensional superconductor TaSe_3 . *Nat. Mater.* **20**, 1093–1099 (2021).
65. Lin, Z.-K. et al. Topological phenomena at defects in acoustic, photonic and solid-state lattices. *Nat. Rev. Phys.* **5**, 483–495 (2023).
66. Hsu, C.-H. et al. Topology on a new facet of bismuth. *Proc. Natl Acad. Sci.* **116**, 13255–13259 (2019).
67. Bruevich, V. & Podzorov, V. Reporting Hall effect measurements of charge carrier mobility in emerging materials. *Nat. Electron.* **7**, 510–512 (2024).
68. Wood, W. A. et al. Revealing contributions to conduction from transport within ordered and disordered regions in highly doped conjugated polymers through analysis of temperature-dependent Hall measurements. *Phys. Rev. Mater.* **7**, 034603 (2023).
69. Chen, C. et al. Boosting thermoelectric performance of semicrystalline conducting polymers by simply adding nucleating agent. *Adv. Mater.* **37**, e2417594 (2025).
70. Chen, C. et al. Observation of weak counterion size dependence of thermoelectric transport in ion exchange doped conducting polymers across a wide range of conductivities. *Adv. Energy Mater.* **13**, 2202797 (2023).
71. Kang, K. et al. Investigation of the thermoelectric response in conducting polymers doped by solid-state diffusion. *Mater. Today Phys.* **8**, 112–122 (2019).
72. Wang, D. et al. Multi-heterojunctioned plastics with high thermoelectric figure of merit. *Nature* **632**, 528–535 (2024).
73. Kang, K. et al. 2D coherent charge transport in highly ordered conducting polymers doped by solid state diffusion. *Nat. Mater.* **15**, 896–902 (2016).
74. Tanaka, H. et al. Thermoelectric properties of a semicrystalline polymer doped beyond the insulator-to-metal transition by electrolyte gating. *Sci. Adv.* **6**, eaay8065 (2020).
75. Venkateshvaran, D. et al. Approaching disorder-free transport in high-mobility conjugated polymers. *Nature* **515**, 384–388 (2014).
76. Jacobs, I. E. et al. Structural and dynamic disorder, not ionic trapping, controls charge transport in highly doped conducting polymers. *J. Am. Chem. Soc.* **144**, 3005–3019 (2022).
77. Tolton, A. & Akšamija, Z. Beneath the disorder: unraveling the impacts of doping on organic electronics and thermoelectrics. *MRS Commun.* **14**, 1054–1061 (2024).
78. Lu, K. et al. Molecular doping-driven modulation of domain charge transport elevates thermoelectric performance in polar polythiophene. *ACS Mater. Lett.* **6**, 4351–4359 (2024).
79. Borup, K. A. et al. Measuring thermoelectric transport properties of materials. *Energy Environ. Sci.* **8**, 423–435 (2015).
80. Iwanaga S., Toberer E. S., LaLonde A., Snyder G. J. A high temperature apparatus for measurement of the seebeck coefficient. *Rev. Sci. Instrum.* **82**, 063905 (2011).

Acknowledgements

Y.L. acknowledges support from the National Natural Science Foundation of China (52273029), the Fujian Science & Technology Innovation Laboratory for Optoelectronic Information of China (2021ZZ119), the Natural Science Foundation of Fujian Province for Distinguished Young Scholars (2023J06045), the Self-deployment Project Research Program of State Key Laboratory of Functional Crystals and Devices (GNJT-2025-ZD07), and the Self-deployment Project Research Program of Haixi Institutes, Chinese Academy of Sciences (CXZX-2023-JQ09). G.J.S. acknowledges support from the National Science Foundation Designing Materials to Revolutionize and Engineer our Future (NSF DMREF #1729487) and award 70NANB19H005 from the U.S. Department of Commerce, National Institute of Standards and Technology as part of the Center for Hierarchical Materials Design (CHi-MaD). This work also benefited from resources provided by the Soft and Hybrid Nanotechnology Experimental (SHyNE) Resource (NSF ECCS-2025633).

Author contributions

Y.L. and G.J.S. conceptualized the idea. Y.L., G.J.S., and X.Z. developed the methodology. X.Z., T.C.C., K.L., M.T.D., M.H., and Y.L. carried out the experimental investigations. Y.L., G.J.S., and X.Z. prepared the visualizations. Y.L. and G.J.S. acquired funding. M.H. coordinated the project administration. Y.L. and G.J.S. supervised the research. Y.L. and X.Z. wrote the original draft. Y.L., G.J.S., X.Z., T.C.C., K.L., M.T.D., and M.H. reviewed and edited the manuscript. All authors contributed to the discussion of the results and provided feedback on the manuscript.

Competing interests

The authors declare no competing interests.

Additional information

Supplementary information The online version contains supplementary material available at <https://doi.org/10.1038/s41467-025-65985-5>.

Correspondence and requests for materials should be addressed to G. Jeffrey Snyder or Yue Lin.

Peer review information *Nature Communications* thanks the anonymous reviewer(s) for their contribution to the peer review of this work. A peer review file is available.

Reprints and permissions information is available at <http://www.nature.com/reprints>

Publisher's note Springer Nature remains neutral with regard to jurisdictional claims in published maps and institutional affiliations.

Open Access This article is licensed under a Creative Commons Attribution-NonCommercial-NoDerivatives 4.0 International License, which permits any non-commercial use, sharing, distribution and reproduction in any medium or format, as long as you give appropriate credit to the original author(s) and the source, provide a link to the Creative Commons licence, and indicate if you modified the licensed material. You do not have permission under this licence to share adapted material derived from this article or parts of it. The images or other third party material in this article are included in the article's Creative Commons licence, unless indicated otherwise in a credit line to the material. If material is not included in the article's Creative Commons licence and your intended use is not permitted by statutory regulation or exceeds the permitted use, you will need to obtain permission directly from the copyright holder. To view a copy of this licence, visit <http://creativecommons.org/licenses/by-nc-nd/4.0/>.

© The Author(s) 2025